

Cabin and Battery Thermal Management of Connected and Automated HEVs for Improved Energy Efficiency Using Hierarchical Model Predictive Control

Mohammad Reza Amini¹, Hao Wang, Xun Gong, Dominic Liao-McPherson¹,
Ilya Kolmanovsky¹, and Jing Sun¹

Abstract—Incorporating traffic information in power management optimization process for electrified and connected vehicles offers opportunities for improving fuel economy. Integrating the management of thermal load (such as those used for heating, ventilation, & air conditioning (HVAC) of the passenger compartment, and for the battery cooling) with the power management process can provide even greater benefits for connected and automated vehicles (CAVs). However, given the relatively slow dynamics associated with the thermal subsystems, the lack of reliable power and thermal loads prediction over an extended prediction horizon is the main challenge for efficient thermal management using model predictive control (MPC). This paper presents a hierarchical two-layer MPC scheme which exploits vehicle speed and traffic preview predictions over short and long prediction horizons to schedule optimal thermal trajectories for the cabin and battery cooling in hybrid electric vehicles (HEVs) via a novel intelligent online constraint handling (IOCH) approach. These trajectories are next incorporated into the vehicle-level controller to determine the proper power split between electric motor and internal combustion engine (ICE). We present the development and experimental validation of control-oriented models used for prediction of the vehicle thermal dynamics and loads over a long planning horizon. Compared to a more traditional single-layer MPC approach, the proposed two-layer MPC shows that depending on the driving cycle and traffic conditions, 2.2% to 5.3% reductions in HEV fuel consumption can be achieved for urban driving and congested city driving cycles, respectively, in CAV operation scenario. This fuel economy improvement is a direct result of taking proactive actions through real-time prediction and optimization to avoid conservative and inefficient thermal responses, while enforcing cabin and battery operating constraints.

Manuscript received July 6, 2018; revised January 30, 2019; accepted June 12, 2019. Manuscript received in final form June 14, 2019. This work was supported by the United States Department of Energy (DOE) through the ARPA-E NEXTCAR Program under Award DE-AR0000797. Recommended by Associate Editor O. Stursberg. (Corresponding author: Mohammad Reza Amini.)

M. R. Amini, H. Wang, X. Gong, and J. Sun are with the Department of Naval Architecture and Marine Engineering, University of Michigan, Ann Arbor, MI 48109 USA (e-mail: mamini@umich.edu; autowang@umich.edu; gongxun@umich.edu; jingsun@umich.edu).

D. Liao-McPherson and I. Kolmanovsky are with the Department of Aerospace Engineering, University of Michigan, Ann Arbor, MI 48109 USA (e-mail: dliao@umich.edu; ilya@umich.edu).

Color versions of one or more of the figures in this paper are available online at <http://ieeexplore.ieee.org>.

Digital Object Identifier 10.1109/TCST.2019.2923792

Index Terms—Battery thermal management (BTM), connected and automated vehicle (CAV) control, hybrid electric vehicle (HEV) energy management, predictive climate control.

NOMENCLATURE

A_f	Vehicle frontal area [m ²].
C_d	Vehicle aerodynamic drag coefficient.
C_{nom}	Battery nominal capacity [Wh].
c_p	Specific heat capacity of air [J/kg · K].
C_r	Vehicle rolling resistance coefficient.
$C_{\text{th, bat}}$	Battery heat capacity. [J/kg · K].
H_l	Long prediction horizon [step].
H_s	Short prediction horizon [step].
I_{bat}	Battery current [A].
m	Vehicle mass [kg].
m_{bat}	Battery mass [kg].
P_{bl}	HVAC blower power [W].
P_{comp}	AC compressor power [W].
P_{fan}	Battery cooling fan power [W].
P_{HVAC}	HVAC system power [W].
P_{trac}	Traction power [W].
R_{bat}	Battery resistance [Ω].
SOC	Battery state of charge [%].
T_{ain}	Cabin inlet flow air temperature [°C].
T_{bat}	Battery pack temperature [°C].
T_{cab}	Cabin air temperature [°C].
T_{evap}	Evaporator wall temperature [°C].
$T_{\text{evap}}^{\text{S.P.}}$	Evaporator wall temperature setpoint [°C].
T_{int}	Cabin interior temperature [°C].
T_s	Sampling time [s].
T_{shell}	Cabin shell temperature [°C].
U_{bat}	Battery voltage [V].
U_{oc}	Battery open-circuit voltage [V].
V_{veh}	Vehicle speed [m/s].
W_{bl}	HVAC blower air flow rate [kg/s].
ϵ	Slack variable [°C].
η_{AC}	HVAC system speed sensitivity coefficient [–].
ω_{fan}	Battery cooling fan speed [rad/s].
ρ	Air density [kg/m ³].

ACRONYMS

AC	Air conditioning.
BTM	Battery thermal management.
CAV	Connected and automated vehicle.
COP	Coefficient of performance.
CSOL	Compressor shutoff logic.
EV	Electric vehicle.
ICE	Internal combustion engine.
IOCH	Intelligent online constraint handling.
iPTM	Integrated power and thermal management.
HEV	Hybrid EV.
HVAC	Heating, ventilation, and AC.
MPC	Model predictive control.
NYCC	New York city cycle.
PHEV	Plug-in HEV.
UDDS	Urban Dynamometer Driving Schedule.
V2I	Vehicle to infrastructure.
V2V	Vehicle to vehicle.

I. INTRODUCTION

EFFICIENT thermal management in electrified vehicles, including HEVs, PHEVs, and pure EVs, is a significant factor in the overall vehicle energy consumption optimization. For HEVs, the cabin air temperature is regulated by an on-board AC system, and the battery temperatures are often controlled by the BTM system using cabin air as the coolant. The AC system consumes a substantial amount of energy in hot summer days, which can significantly compromise the vehicle overall energy efficiency and driving range [1]. It has been estimated that, in the United States, about 7 billion gallons of fuel are consumed per year just to power the AC systems for light-duty vehicles [2]. A study performed at the Argonne National Lab (ANL) showed a 53.7% reduction in vehicle driving range due to AC for Ford Focus EV, tested over the UDDS [1]. Moreover, since the required energy to drive the AC compressor, blower, fans, and so on is provided by the battery, optimizing the cabin and battery cooling loads during hot weather is essential for improving the overall vehicle energy efficiency.

While extensive studies have been carried out on fuel economy optimization for electrified vehicles (see [3], [4] and the references therein), efficient thermal management of electrified connected and automated vehicles (CAVs) has not been fully explored. Most previous research efforts [5], [6] have addressed the thermal management problems associated with the AC system for ICE powered vehicles with belt-driven compressors. For electrified vehicles, however, the compressor of the AC system is electrically driven and directly draws power from high-voltage battery, thereby interacting with other power loads such as the traction power. While the benefits of MPC-based AC optimization for HEVs [7], [8] and EVs [9] have been studied recently, challenges and opportunities in integrating traffic preview in CAVs have not been fully explored.

Another important aspect of electrified vehicle thermal management is that the required heat flow for active BTM is provided through a combination of air and liquid cooling

loops. The coolant of the liquid-based BTM system dissipates the rejected heat from the battery to the refrigerant of the AC system via a heat exchanger. The air cooling regulates the battery temperature by blowing the compartment air into the battery pack using a fan. Since the cabin air is cooled by the AC compressor, the battery air cooling loop is also coupled to the vehicle HVAC system. Thus, the BTM system also interacts with the AC and, consequently, with other vehicle power loads. While the application of optimization techniques has been pursued in the literature for active BTM of electrified vehicles [10]–[14] and the dependencies of the BTM strategy on the driving cycle and vehicle speed have been studied, the coupling between cabin and BTM and sensitivity of the BTM performance to cabin air temperature and its impact on fuel economy have not been evaluated.

Unlike power system with fast dynamics, the response of the thermal subsystem is slow due to large thermal inertia and its optimization requires a long prediction/planning horizon. While the vehicle speed and demanded traction power can be accurately predicted over a short time horizon, longer horizon prediction necessary for thermal management using V2V and V2I information is subject to greater uncertainties. Hence, a control system is necessary that 1) can capitalize on the connectivity technology to improve the energy efficiency and 2) be able to handle the uncertainties in the long horizon vehicle speed and traffic events predictions. Moreover, real-time implementation requirements dictate that accurate and simple models are used on-board to predict the thermal dynamics and loads over a long prediction horizon.

In this paper, we propose a novel two-layer hierarchical MPC framework for cabin and BTM for an HEV that addresses the above-mentioned requirements. It was shown that, in [7], the AC system is sensitive to vehicle speed, which provides the motivation to incorporate traffic information and vehicle speed preview into the iPTM. In this paper, we extend the AC system sensitivity analysis to generate an AC efficiency map, which will be exploited to optimize AC cooling loads on the battery based on preview information. While the impact of AC load on the fuel economy is significant [1], [2], the energy saving potential is constrained by the requirement of the passenger comfort. Additional fuel economy gains may be possible with some compromise of the passenger comfort [15]; however, we do not pursue such an approach in this paper, focusing instead on the benefits of exploiting the preview information in CAVs without compromising the customer comfort.

The two-layer hierarchical MPC approach we are taking is inspired, in part, by the recent works in the literature on multi-layer optimization and prediction for systems with multiple time scales, including microgrids [16], [17], power flow [18], chemical plants [19], and building energy management [20] systems. Hierarchical MPC allows for simultaneous planning of thermal trajectories over a long horizon, and steering the system states toward the planned trajectories over a short horizon. The two layers of the proposed hierarchical MPC are referred to as scheduling layer and a piloting layer. In the scheduling layer, a long prediction horizon is used to account for the relatively slow dynamics of the cabin temperature

and plan optimized thermal trajectories. A fast model predictive controller with much shorter prediction horizon and fewer optimization variables and constraints is implemented in the piloting layer to track the planned thermal trajectories aiming at reducing power consumption. By responding to the preview of traffic conditions that inform the predicted vehicle speed profile, the proposed two-layer MPC manages the power used for cooling the cabin so that the powertrain system and associated subsystems operate efficiently, thereby optimizing the overall system efficiency for different driving scenarios.

The contributions of this paper are threefold. First, control-oriented models of cabin and battery temperatures, to be used for prediction in MPC, are developed and experimentally validated. Second, a hierarchical two-layer MPC for cabin and BTM equipped with a novel IOCH approach is proposed. Third, given the uncertainties associated with long-term prediction of vehicle speed profile, a novel methodology is developed to combine the short-horizon vehicle speed predictions that can be generated on-board of a CAV with an estimated traffic flow information over a longer horizon. The fuel saving potential of the proposed two-layer MPC thermal management strategy, even with imperfect preview information, is demonstrated on the high-fidelity simulation models over urban and congested city driving cycles.

This paper is organized as follows. In Section II, the control-oriented predictive models for HEV cabin and battery thermal systems are developed and validated against experimental data and high-fidelity physics-based simulation model. In Section III, centralized and decentralized single-layer MPC solutions for cabin and BTM are presented. Based on the results of Section III, in Section IV, a hierarchical two-layer MPC framework for AC control with preview information incorporated over a long prediction horizon is proposed. Moreover, the IOCH and AC CSOL are explained. Next, the traffic flow model for long horizon prediction is introduced in Section V, and the effect of uncertainties associated with the vehicle speed prediction on the thermal management system is discussed. The two-layer MPC controller is also implemented in a rapid prototyping system to demonstrate its real-time feasibility. Section VI reports the results of implementing the proposed two-layer MPC for cabin and BTM in simulations and discusses the achieved energy savings at the vehicle level. Finally, concluding remarks are presented in Section VII.

II. CONTROL-ORIENTED THERMAL MODELING

In this section, control-oriented thermal models for both AC and battery systems are developed and then validated against a high-fidelity simulation model (CoolSim) and experimental vehicle data. The overall schematic of an HEV thermal system, including the AC and BTM loops, is shown in Fig. 1. As can be observed, the battery power (P_{bat}) is used to partly satisfy the traction power demand and is also consumed by the AC compressor (P_{comp}), blower (P_{bl}), and battery cooling fan (P_{fan}). The AC loop draws power from the battery to cool the cabin air temperature (T_{cab}), which is then used for cooling the battery via the battery cooling fan.

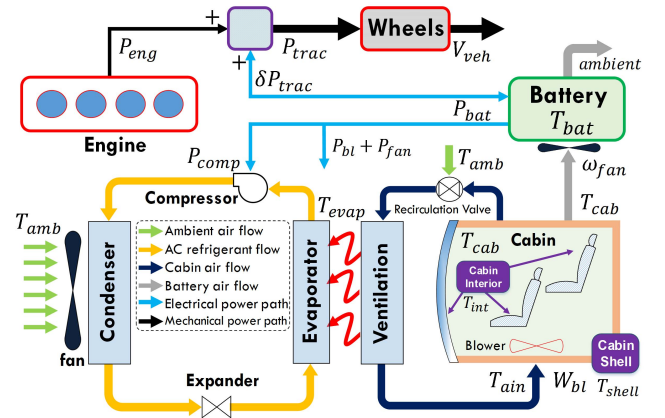


Fig. 1. Schematic of HEV thermal and power loops.

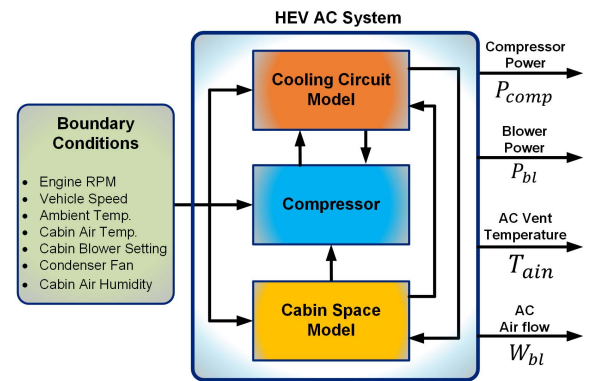


Fig. 2. Structure of the CoolSim simulink model.

A. Air Conditioning System Predictive Model

1) *High-Fidelity CoolSim Model*: Based on a high-fidelity simulation model for passenger car AC system, CoolSim,¹ a control-oriented model has been developed for predicting the cabin and evaporator wall temperatures of the vehicle AC system. Fig. 2 shows the schematic of the CoolSim model with four major subcomponents: 1) the boundary condition block, which provides the speed profiles and ambient conditions such as temperature and pressure; 2) the cooling circuit block, which consists of detailed models of the evaporator, condenser, condenser fan, evaporator valve, and connecting pipes; 3) the compressor block, which, as the primary energy consumer in the AC system, is modeled separately from the cooling circuit; and 4) the cabin space block, which models the thermal dynamics of the cabin. See [21] for the modeling details of each subcomponent. This model is capable of simulating cycle-by-cycle behavior of the AC system and has been validated versus experimental data in [21]. While both electrically driven and belt-driven compressor configurations are available, the electrically driven one is used for the HEV AC system under consideration.

2) *Control-Oriented AC System Predictive Model*: The control-oriented model that will be used for prediction of

¹CoolSim is a MATLAB/Simulink-based open-source modeling environment available from National Renewable Energy Lab (NREL) [21], [22].

AC system response by MPC has the following form [7]:

$$\begin{aligned} T_{\text{cab}}(k+1) &= f_{T_{\text{cab}}}(k) = T_{\text{cab}}(k) \\ &+ \gamma_1(T_{\text{int}}(k) - T_{\text{cab}}(k)) \\ &+ \gamma_2(T_{\text{shell}}(k) - T_{\text{cab}}(k)) \\ &+ \gamma_3(T_{\text{shell}}(k) - T_{\text{cab}}(k))W_{\text{bl}}(k) + \tau_1 \end{aligned} \quad (1)$$

$$\begin{aligned} T_{\text{evap}}(k+1) &= f_{T_{\text{evap}}}(k) = \gamma_4 T_{\text{evap}}(k) \\ &+ \gamma_5(T_{\text{evap}}(k) - T_{\text{evap}}^{\text{s.p.}}(k)) + \tau_2 \end{aligned} \quad (2)$$

$$T_{\text{shell}}(k) = \gamma_6 T_{\text{evap}}(k) + \gamma_7 W_{\text{bl}}(k) + \tau_3 \quad (3)$$

where T_{cab} , T_{int} , T_{shell} , T_{evap} , and T_{shell} represent the temperatures of the cabin air, the cabin interior (e.g., seats and panels), the cabin shell, the evaporator wall, and the cabin inlet flow air temperature (all in K), respectively (see Fig. 1). The control inputs to the model are W_{bl} (blower flow rate) and $T_{\text{evap}}^{\text{s.p.}}$ (evaporator wall temperature setpoint). The model parameters γ_p ($p = 1, 2, \dots, 7$) and τ_q ($q = 1, 2, 3$) are constants that are identified by matching the response to the one of CoolSim model. As can be observed in (1), due to the multiplicative coupling between the input (W_{bl}) and states (T_{shell} , T_{cab}), the overall AC model (1)–(3) is nonlinear.

The simulated outputs from CoolSim, which are sampled every 5 s, are utilized to identify the unknown parameters in (1)–(3) by using the least-squares technique. The resulting identified parameters are $\gamma = [\gamma_1 \ \gamma_2 \ \dots \ \gamma_7] = [0.245 \ 0.087 \ 1.299 \ 1.004 \ -0.517 \ 0.455 \ 34.957]$ and $\tau = [\tau_1 \ \tau_2 \ \tau_3] = [-0.184 \ -1.322 \ 154.499]$. Fig. 3 shows the validation results of the control-oriented model initialized to match the measurements only at the initial time step with T_{int} and T_{shell} provided as the external inputs to the model. Over 300 steps (1500 s), Fig. 3 indicates that the identified model (1)–(3) provides reasonably accurate predictions.

Two major energy consumers in the AC system are the compressor and the blower. According to [23], their power consumption can be estimated by

$$\begin{aligned} P_{\text{comp}} &= \frac{c_p}{\eta_{\text{cop}}} W_{\text{bl}}(T_{\text{amb}} - T_{\text{shell}}) \\ &= \frac{c_p}{\eta_{\text{cop}}} W_{\text{bl}}(T_{\text{amb}} - \gamma_6 T_{\text{evap}} - \gamma_7 W_{\text{bl}} - \tau_3) \end{aligned} \quad (4)$$

$$P_{\text{bl}} = \beta_1 W_{\text{bl}}^2 + \beta_2 W_{\text{bl}} + \beta_3 \quad (5)$$

where P_{comp} and P_{bl} represent the powers of the compressor and blower, respectively, $c_p = 1008 \text{ J/kg}\cdot\text{K}$ is the specific heat capacity of air at constant pressure, $\eta_{\text{cop}} = 3.5$ is the COP of the AC system [24], and $[\beta_1 \ \beta_2 \ \beta_3] = [24156 \ -1974.2 \ 49.318]$ are the parameters identified from CoolSim data [7].

B. Battery Thermal and Electrical Models

The high-fidelity battery temperature models such as given in [25] and [26] are too complex to be used as the prediction model for MPC. Thus, we propose and subsequently validate a simplified control-oriented battery temperature model based on the experimental data collected from a 2017 HEV Prius

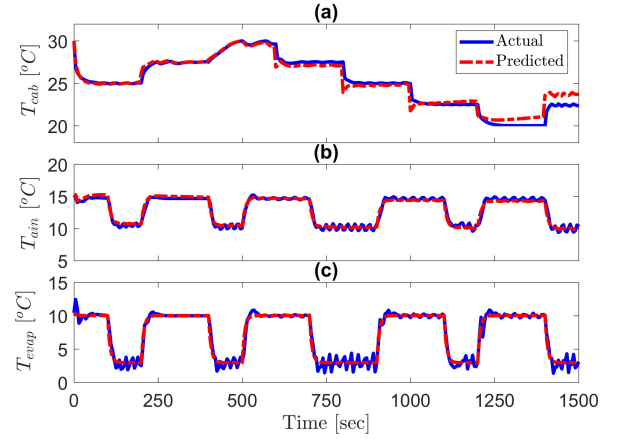


Fig. 3. Validation results of the control-oriented AC system prediction model.

test vehicle. This model has the following structure:

$$\begin{aligned} \dot{T}_{\text{bat}}(t) &= \frac{I_{\text{bat}}^2 R_{\text{bat}}}{m_{\text{bat}} C_{\text{th,bat}}} \\ &- \begin{cases} A_1(T_{\text{bat}} - T_{\text{cab}})\omega_{\text{fan}}^{0.8} \left(1 - \exp\left(\frac{A_2}{\omega_{\text{fan}}}\right)\right) & \text{if } \omega_{\text{fan}} \neq 0 \\ \frac{T_{\text{bat}} - T_{\text{cab}}}{m_{\text{bat}} C_{\text{th,bat}} R_{\text{th}}} & \text{if } \omega_{\text{fan}} = 0 \end{cases} \end{aligned} \quad (6)$$

where T_{bat} , I_{bat} , and R_{bat} are the battery temperature, current, and internal resistance, respectively. The battery pack is considered as a lumped mass (m_{bat}) with heat capacity $C_{\text{th,bat}}$. A_1 and A_2 are the constant parameters, ω_{fan} is the rotational speed of the battery cooling fan, and R_{th} is the equivalent thermal resistance associated with conduction and natural convection [25], [27].

As can be seen from (6), the time rate of change of battery temperature is a function of the battery fan rotation speed (which determines the cooling air speed through the battery pack according to the fan geometry), cabin air temperature (T_{cab}), and also the battery current (I_{bat}). The parameters of the control-oriented battery thermal model in (6) are identified based on the experimental data collected from the test vehicle. The BTM system of the test vehicle has been partially instrumented to obtain access to the data being communicated over the controlled area network (CAN) via the on-board diagnostics port.

The vehicle was driven at different speeds, with different cabin air temperatures. Fig. 4(a)–(d) show the experimental measurements of the inputs (T_{cab} , ω_{fan} , V_{veh} , and I_{bat}), and Fig. 4(e) illustrates the output (T_{bat}). The first half of the data are being used for identifying the model parameters, and the second half are utilized for verification of the model. Fig. 4 confirms the capability of the proposed model (6) to predict the battery temperature accurately. It should be noted that the plotted battery temperature in Fig. 4(e) is the average of the recorded temperature signals from six modules of the HEV battery that represents the average temperature of the whole battery pack. Based on the model identification results, the parameters of the control-oriented battery temperature model in (6) are $A_1 = 2.6711 \times 10^{-5}$ and $A_2 = -2.6763 \times 10^3$.

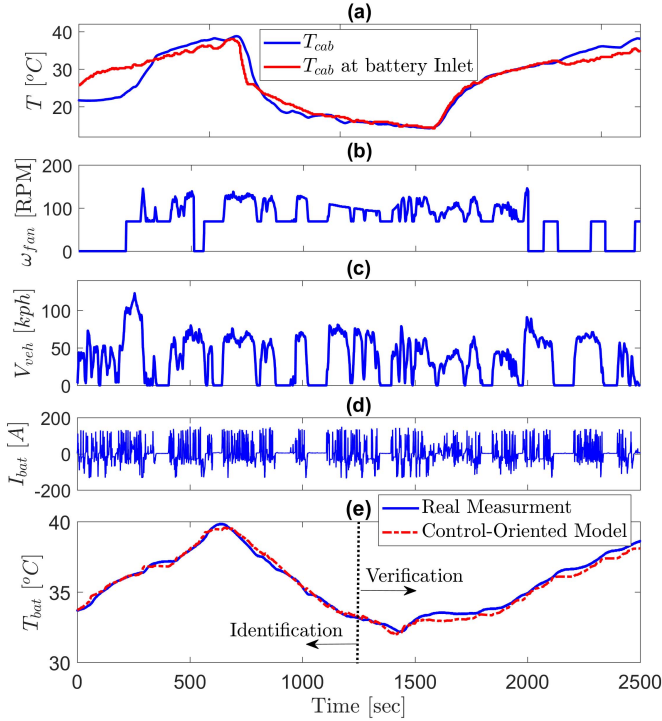


Fig. 4. Experimental data used for battery thermal model identification and validation. (a) Cabin temperature and air temperature at the battery pack inlet. (b) Battery fan rotational speed. (c) Vehicle speed. (d) Battery current. (e) Real battery temperature measurement versus the control-oriented model. The first half of the data were used for model identification, while the second half were utilized to validate the model.

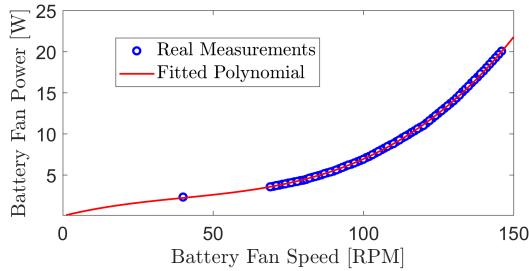


Fig. 5. Measured and modeled battery fan power consumption as a function of battery fan rotational speed. Experimental data set used is the same as shown in Fig. 4.

Fig. 4(e) shows that the proposed model (6) can predict T_{bat} with a prediction error of less than $0.5\text{ }^{\circ}\text{C}$. As a conclusion, the control-oriented model (6) provides acceptable prediction for T_{bat} as a function of I_{bat} , ω_{fan} , and T_{cab} .

The battery cooling fan power (P_{fan}) is modeled as a function of the fan rotation speed (ω_{fan}). Fig. 5 shows the experimental data for the battery fan power and rotational speed over the driving cycle shown in Fig. 4. A polynomial model is fitted to the experimental data as shown in Fig. 5 to estimate P_{fan} as a function of ω_{fan} , which is an input to the battery temperature model (6)

$$P_{fan} = \alpha_1 \omega_{fan}^3 + \alpha_2 \omega_{fan}^2 + \alpha_3 \omega_{fan} + \alpha_4 \quad (7)$$

where $\alpha_1 = 1.191 \times 10^{-5}$, $\alpha_2 = -0.00144$, $\alpha_3 = 0.09399$, and $\alpha_4 = 1.195 \times 10^{-5}$.

The battery current can be written as a function of the total demanded electrical power as follows:

$$I_{bat} = (\delta P_{trac} + P_{HVAC} + P_{fan})/U_{bat} \quad (8)$$

where U_{bat} is the battery voltage, P_{trac} is the demanded traction power, P_{HVAC} is the total power consumed by the HVAC system via the electric AC compressor and HVAC blower, and P_{fan} is the required power for the battery cooling fan to provide the specified heat flow rate for the battery heating/cooling. It is assumed in (8) that P_{trac} , P_{HVAC} , and P_{fan} are the main power loads on the battery, and other auxiliary loads on the battery are neglected. The variable δ in (8) is the power split coefficient between the battery and ICE, determined by the vehicle hybrid control module. Note that U_{bat} can be expressed as a function of the open-circuit voltage (U_{oc}), R_{bat} , and I_{bat}

$$U_{bat} = U_{oc} - I_{bat} R_{bat} \quad (9)$$

where U_{oc} and R_{bat} are functions of the battery state of charge (SOC) and T_{bat} . By substituting U_{bat} in (9) with $(\delta P_{trac} + P_{HVAC} + P_{fan})/I_{bat}$ from (8), I_{bat} can be expressed as

$$I_{bat}(t) = \frac{U_{oc} - \sqrt{U_{oc}^2 - 4R_{bat}(\delta P_{trac} + P_{HVAC} + P_{fan})}}{2R_{bat}} \quad (10)$$

Moreover, SOC dynamics are governed by

$$\dot{SOC}(t) = -\frac{I_{bat}}{C_{nom}} \quad (11)$$

where C_{nom} is the nominal capacity of the battery. The demanded traction power can be estimated as [28]

$$P_{trac} = V_{veh}(F_r + F_a + m\dot{V}_{veh}) \quad (12)$$

where V_{veh} and m are the vehicle speed and mass, respectively. The rolling (F_r) and aerodynamic (F_d) resistance forces are calculated as follows:

$$F_r = C_r mg \quad (13)$$

$$F_d = 0.5\rho A_f C_d V_{veh}^2 \quad (14)$$

where C_r and C_d are, respectively, the rolling resistance and aerodynamic drag coefficients, A_f is the vehicle frontal area, and ρ is the air density. In this paper, the road grade is assumed to be zero. The parameters of the vehicle longitudinal dynamics and lookup tables of the battery electrical model [e.g., $R_{bat}(SOC, T_{bat})$ and $U_{oc}(SOC, T_{bat})$] are adopted from Autonomie² software library for the Toyota Prius. These parameters are listed in the Appendix.

Fig. 5 shows that, compared to the traction and AC powers that will be discussed later, P_{fan} is relatively small ($< 25\text{ W}$). It should be noted that while P_{fan} is negligible for the Prius HEV with only air cooling BTM system, for PHEVs and pure EVs with larger high-voltage batteries, and with both air and liquid battery cooling, the battery cooling load could be much higher. The coolant of the liquid cooling system in such vehicles is usually cooled by an electric AC compressor. Unlike P_{fan} , the AC compressor power consumption has a significant effect on the battery energy consumption and, consequently, on the vehicle fuel economy.

²Autonomie is a MATLAB/Simulink-based system simulation tool for vehicle energy consumption and performance analysis developed by ANL [26]

III. CABIN AND BATTERY PREDICTIVE THERMAL MANAGEMENT

For the cooling scenario during hot summer, when the initial temperatures of the battery and cabin air are above the acceptable/comfort range, the control objectives of the HEV cabin and BTM system are to: 1) reduce the cabin air temperature and maintain it within a predefined comfort zone with respect to a setpoint ($T_{\text{cab}}^{\text{s.p.}}$), which is commanded by the passenger; 2) cool down the battery pack and maintain battery temperature T_{bat} at the desired setpoint $T_{\text{bat}}^{\text{s.p.}}$ while heat is constantly generated when power is drawn from the battery; and 3) minimize the cumulative AC and BTM systems power consumption determined by P_{comp} , P_{bl} , and P_{fan} . The cabin and BTM controller are designed based on MPC with the control-oriented thermal models developed in Section II.

We first consider a centralized MPC design and then introduce a decentralized MPC design with which it is easier to avoid adverse interactions between cabin and BTM loops. In order to accommodate the long horizon vehicle speed preview informed by traffic flow information in the dynamic optimization, further reformulation of the AC controller of the decentralized MPC design will be made to a two-layer architecture with the scheduling and piloting layers in Section IV.

A. Centralized Controller Design

The cabin and BTM objectives can be addressed by formulating a centralized constrained nonlinear MPC problem over a finite-time prediction horizon (N) with $T_{\text{evap}}^{\text{s.p.}}$, W_{bl} , and ω_{fan} being the optimization variables

$$\begin{aligned} \arg \min_{\substack{T_{\text{evap}}^{\text{s.p.}}(\cdot|k) \\ W_{\text{bl}}(\cdot|k) \\ \omega_{\text{fan}}(\cdot|k)}} \sum_{i=0}^N & \left\{ \begin{array}{l} P_{\text{comp}}(i|k) + P_{\text{bl}}(i|k) + P_{\text{fan}}(i|k) \\ + w_c (T_{\text{cab}}(i|k) - T_{\text{cab}}^{\text{s.p.}})^2 \\ + w_b (T_{\text{bat}}(i|k) - T_{\text{bat}}^{\text{s.p.}})^2 \end{array} \right\} \\ \text{s.t. } & T_{\text{cab}}(i+1|k) = f_{T_{\text{cab}}}(i|k), \quad i = 0, \dots, N \\ & T_{\text{evap}}(i+1|k) = f_{T_{\text{evap}}}(i|k), \quad i = 0, \dots, N \\ & T_{\text{bat}}(i+1|k) = f_{T_{\text{bat}}}(i|k), \quad i = 0, \dots, N \\ & T_{\text{bat}}^{\text{LL}} \leq T_{\text{bat}}(i|k) \leq T_{\text{bat}}^{\text{UL}}, \quad i = 0, \dots, N \\ & T_{\text{cab}}^{\text{LL}} \leq T_{\text{cab}}(i|k) \leq T_{\text{cab}}^{\text{UL}}, \quad i = 0, \dots, N \\ & T_{\text{evap}}^{\text{LL}} \leq T_{\text{evap}}(i|k) \leq T_{\text{evap}}^{\text{UL}}, \quad i = 0, \dots, N \\ & 0 \leq \omega_{\text{fan}}(i|k) \leq 200 \text{ r/min}, \quad i = 0, \dots, N-1 \\ & 0.05 \text{ kg/s} \leq W_{\text{bl}}(i|k) \leq 0.15 \text{ kg/s}, \quad i = 0, \dots, N-1 \\ & 3 \text{ }^\circ\text{C} \leq T_{\text{evap}}^{\text{s.p.}}(i|k) \leq 10 \text{ }^\circ\text{C}, \quad i = 0, \dots, N-1 \\ & T_{\text{cab}}(0|k) = T_{\text{cab}}(k), \quad T_{\text{evap}}(0|k) = T_{\text{evap}}(k) \\ & T_{\text{bat}}(0|k) = T_{\text{bat}}(k) \end{aligned} \quad (15)$$

where $(i|k)$ designates the predicted value at the time instant $k+i$ when the prediction is made at the time instant k . The nonlinear MPC optimization problem (15) is to minimize the cumulative power spent for cabin (P_{comp} , P_{bl}) and BTM (P_{fan}) over the prediction horizon N while enforcing the imposed state and input constraints. The numerical values of the state and input constraints in (15) are selected according to the operation limits of the CoolSim model and test vehicle

BTM system for AC and battery systems, respectively. The parameters $T_{\text{bat}}^{\text{UL}}$ and $T_{\text{bat}}^{\text{LL}}$ are the upper and lower limits of the battery operating temperature, and they are set to 40 °C and 20 °C, respectively. The parameters $T_{\text{cab}}^{\text{UL}}$ and $T_{\text{cab}}^{\text{LL}}$ are the upper and lower limits on the cabin temperature, which define the comfort zone inside the cabin. $T_{\text{cab}}^{\text{LL}}$ is set to 24 °C, while $T_{\text{cab}}^{\text{UL}}$ is variable. Furthermore, $T_{\text{evap}}^{\text{UL}} = 12 \text{ }^\circ\text{C}$ and $T_{\text{evap}}^{\text{LL}} = 0 \text{ }^\circ\text{C}$ are the upper and lower limits of the evaporator wall temperature. Due to the coupling between the cabin and battery temperatures, and the economic terms in the MPC cost function (i.e., terms corresponding to P_{comp} , P_{bl} , and P_{fan}), constraints should be imposed on both cabin and battery temperatures to ensure they remain within the desired range. The weights for tracking the cabin and battery temperature setpoints are denoted by w_c and w_b , respectively. The functions $f_{T_{\text{cab}}}$ and $f_{T_{\text{evap}}}$ are used to represent the dynamics of T_{cab} and T_{evap} defined by (1)–(3). The function $f_{T_{\text{bat}}}$ represents the dynamics of T_{bat} in discrete time, and it is obtained by applying Euler forward method to (6) with a sampling time of $T_s = 5 \text{ s}$.

The MPC feedback law is defined by the first elements $T_{\text{evap}}^{\text{s.p.}}(0|k)$, $W_{\text{bl}}(0|k)$, and $\omega_{\text{fan}}(0|k)$ of the optimal solution sequence to (15). The MPC simulation is carried out on a desktop computer, with an Intel Core i7@2.60 GHz processor, in MATLAB/SIMULINK using YALMIP [29] for formulating the optimization problem and interior point optimizer [30] for solving the optimization problem numerically. It is noted that for HEVs with the air cooling BTM system, because the power consumed for operating the battery cooling actuator (P_{fan}) is negligible as compared to the AC compressor P_{comp} , the design of a BTM controller in tracking ($w_b \neq 0$) or economic ($w_b = 0$) schemes leads to similar energy consumption results. Thus, in order to simplify the BTM system design and better battery conditioning [27], [31], instead of letting the battery temperature to vary within a specific range ($w_b = 0$), a constant setpoint ($T_{\text{bat}}^{\text{s.p.}}$) has been chosen to be tracked in (15) with $w_b \neq 0$. This appears to also improve the numerical conditioning of the problem.

Fig. 6 shows the performance of the centralized MPC (15) on the control-oriented models for tracking $T_{\text{bat}}^{\text{s.p.}}$ while enforcing the cabin temperature to be within the shown comfort zone when $w_c = 0$ over UDSS, which represents city driving conditions. Moreover, for the centralized and decentralized MPCs in this section and shown in Fig. 6, it is assumed that the perfect time-varying vehicle speed preview is known over the prediction horizon.

Remark: The reason for selecting $w_c = 0$ in this simulation is to demonstrate the coupling between the battery and cabin air temperatures when the system is controlled by the centralized controller. Note that if tracking of $T_{\text{bat}}^{\text{s.p.}}$ is not enforced, i.e., $w_c = 0$, the centralized MPC (15) has the authority to vary the cabin temperature within the comfort zone for cooling the battery. The sampling time and the prediction horizon of the MPC in (15) are set to $T_s = 5 \text{ s}$ and $N = 6$ (30 s), respectively.

In all the simulations presented in this section, the demanded fraction of traction power from the battery (δP_{trac}) is extracted from the Prius HEV model over UDSS

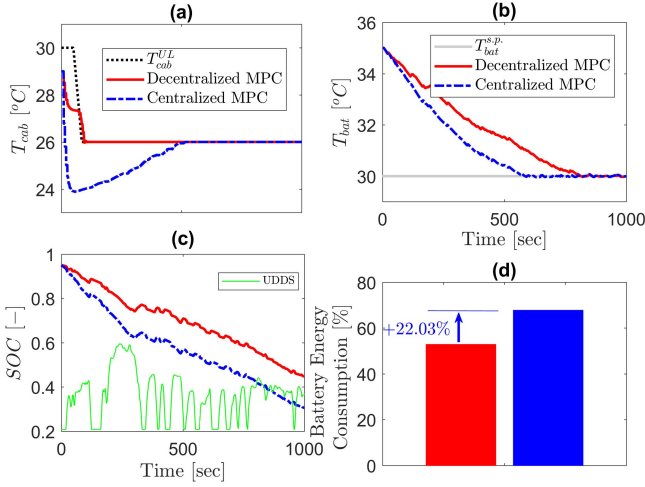


Fig. 6. Results of BTM and cabin temperature control by using the centralized and decentralized MPCs implemented on the control-oriented models. (a) T_{cab} . (b) T_{bat} . (c) Time histories of SOC and vehicle speed over UDDS. (d) Battery energy consumption. $N = N_1 = N_2 = 6$ (30 s).

in the Autonomie software and is assumed to be the same. Therefore, the impact of BTM and AC systems on the HEV battery energy consumption can be evaluated explicitly. In Section VI, this assumption on δP_{trac} will be relaxed, and the controller will be implemented at the vehicle level in order to quantify the overall vehicle fuel economy benefits.

If a relatively large w_b is selected in (15) for the battery temperature setpoint tracking while $w_c = 0$, it can be observed from Fig. 6(a) that the MPC commands the AC compressor to reduce the cabin temperature below T_{cab}^{UL} . While this could result in faster battery temperature cooling [Fig. 6(b)], compared to the case where a relatively small w_b is selected, the battery energy consumption will increase considerably due to the rise in the AC power demand. The percentage of the battery energy consumption in Fig. 6(d) is calculated with respect to the change in the battery SOC at the end of the driving cycle ($SOC(k_f)$) compared to the initial SOC ($SOC(0)$)

$$\text{Battery Energy Consumption [\%]} = \frac{SOC(0) - SOC(k_f)}{SOC(0)} \times 100. \quad (16)$$

B. Decentralized Controller Design

The AC compressor power demand is much higher than the required power for the battery cooling fan (Fig. 5). As shown in Section III-A, if T_{cab} becomes driven by T_{bat} , this could increase the battery energy consumption. One approach to avoid BTM system affecting the cabin temperature and AC system is to select a small value for w_b . However, this could result in poor battery temperature setpoint tracking. The second approach is to decouple the BTM and AC controllers by designing a decentralized MPC.

The decentralized MPC solution for the BTM and AC control not only guarantees desirable $T_{bat}^{s.p.}$ tracking but also

avoids any increase in the AC power demand for battery cooling purpose. Moreover, the decentralized MPC solution reduces the controller design complexity as it has fewer tuning parameters and lower computation cost.

The decentralized MPC for BTM system is based on the solution of the following optimization problem:

$$\begin{aligned} \arg \min_{\omega_{fan}(\cdot|k)} \sum_{i=0}^{N_1} P_{fan}(i|k) + w_b (T_{bat}(i|k) - T_{bat}^{s.p.})^2 \\ \text{s.t. } T_{bat}(i+1|k) = f_{T_{bat}}(i|k), \quad i = 0, \dots, N_1 \\ T_{bat}^{LL} \leq T_{bat}(i|k) \leq T_{bat}^{UL}, \quad i = 0, \dots, N_1 \\ 0 \leq \omega_{fan}(i|k) \leq 200 \text{ r/min}, \quad i = 0, \dots, N_1 - 1 \\ T_{bat}(0|k) = T_{bat}(k) \end{aligned} \quad (17)$$

and, for the AC system, the decentralized MPC has the following form:

$$\begin{aligned} \arg \min_{\substack{T_{evap}^{s.p.}(\cdot|k) \\ W_{bl}(\cdot|k)}} \sum_{i=0}^{N_2} \left\{ P_{comp}(i|k) + P_{bl}(i|k) \right. \\ \left. + w_c (T_{cab}(i|k) - T_{cab}^{s.p.})^2 \right\} \\ \text{s.t. } T_{cab}(i+1|k) = f_{T_{cab}}(i|k), \quad i = 0, \dots, N_2 \\ T_{evap}(i+1|k) = f_{T_{evap}}(i|k), \quad i = 0, \dots, N_2 \\ T_{cab}^{LL} \leq T_{cab}(i|k) \leq T_{cab}^{UL}, \quad i = 0, \dots, N_2 \\ T_{evap}^{LL} \leq T_{evap}(i|k) \leq T_{evap}^{UL}, \quad i = 0, \dots, N_2 \\ 0.05 \text{ kg/s} \leq W_{bl}(i|k) \leq 0.15 \text{ kg/s}, \quad i = 0, \dots, N_2 - 1 \\ 3 \text{ }^\circ\text{C} \leq T_{evap}^{s.p.}(i|k) \leq 10 \text{ }^\circ\text{C}, \quad i = 0, \dots, N_2 - 1 \\ T_{cab}(0|k) = T_{cab}(k), \quad T_{evap}(0|k) = T_{evap}(k) \end{aligned} \quad (18)$$

where N_1 and N_2 are the prediction horizons for the decentralized BTM and AC MPCs, respectively.

Fig. 6(a) shows that the AC MPC (18) follows T_{cab}^{UL} (when $w_c = 0$), which minimizes the AC power consumption. Compared to the centralized MPC scheme, it can be observed from Fig. 6(b) that while $T_{bat}^{s.p.}$ tracking is achieved, the decentralized MPC results in slower battery cooling rate, as the cabin temperature is higher on average. For the decentralized BTM MPC (17), the average battery temperature is 1.5% higher than with the centralized MPC. On the other hand, it can be seen in Fig. 6(d) that the decentralized MPC consumes less power compared to the centralized MPC. The advantages of the decentralized design are summarized as follows.

- 1) The impact of T_{bat} on T_{cab} is reduced; therefore, the battery temperature is decoupled from the passenger comfort.
- 2) The BTM and AC MPCs can employ different prediction horizons (N_1, N_2) and different sampling rates, which helps to accommodate the difference in the cabin temperature and battery temperature time constants and reduce the computation time.
- 3) It allows for simpler controller tuning and easier implementation.

In the remainder of this paper, the decentralized MPC in (17) with $N_1 = 6$ (30 s) is considered for BTM, while the AC MPC (18) is further enhanced by incorporating vehicle speed preview information to improve the overall vehicle energy efficiency. The nominal architecture of the decentralized

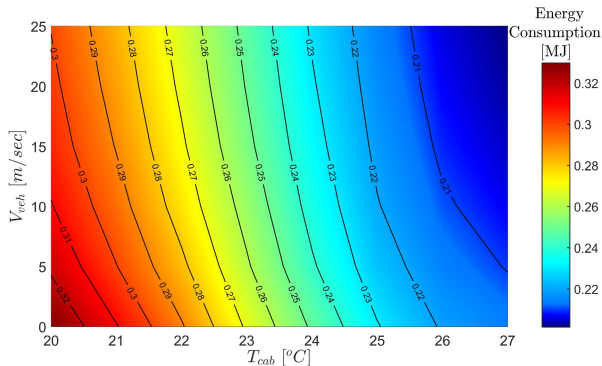


Fig. 7. AC compressor energy consumption map as a function of the cabin temperature setpoint and vehicle speed at constant travel time.

MPC (17), (18) is referred to as the single-layer MPC. We use it as a benchmark for comparison as it would typically represent a more traditional approach to MPC implementation for thermal management.

IV. INCORPORATION OF TRAFFIC INFORMATION INTO AC THERMAL MANAGEMENT

The first step to design an energy-optimal controller for the AC system with respect to traffic information is to quantify the sensitivity of the system to the vehicle speed. To this end, a sensitivity analysis of the AC system energy consumption is performed by using the CoolSim model at different constant vehicle speeds ($V_{\text{veh}} = 0, 5, 10, 15, 20,$ and 25 m/s) and different cabin air temperature setpoints ($T_{\text{cab}}^{\text{s.p.}} = 20, 21, \dots, 27$ °C) for a fixed travel time of 200 s. The results of the sensitivity analysis shown in Fig. 7 indicate that at the same $T_{\text{cab}}^{\text{s.p.}}$, the efficiency of the AC system increases as the vehicle speed increases. This observation is consistent with the underlying physics, as the effective ram air speed through the condenser increases as vehicle speed increases, so that the condenser dissipates the heat faster, which leads to higher overall efficiency for the AC system.

It is observed in Fig. 7 that depending on $T_{\text{cab}}^{\text{s.p.}}$, the AC system energy consumption increases by 7%–10% when the vehicle speed decreases from 25 to 0 m/s over the same time interval of travel. The sensitivity of the AC system to vehicle speed is even more pronounced if considering energy consumption normalized by the traveling distance. It can be shown that the normalized energy consumption can increase up to five times when the vehicle speed changes from 25 to 5 m/s for different $T_{\text{cab}}^{\text{s.p.}}$. A vehicle traveling at higher speed spends less time to cover the same distance, reducing the AC operating time and thus the associated energy consumption. We note that the AC energy consumption in hot weather conditions can be up to a third of average traction power in city driving.

The single-layer MPC (18) tracks a constant setpoint ($T_{\text{cab}}^{\text{s.p.}}$) and uses a vehicle speed independent prediction model; hence, it is not able to exploit the energy saving potential associated with the AC system sensitivity to vehicle speed. The two-layer solution uses a scheduling layer MPC at the upper layer and a piloting layer MPC at the lower layer. The scheduling layer MPC first calculates the energy efficient trajectories for

the AC system while accounting for the vehicle speed preview informed by future traffic information. These scheduled trajectories are passed on to the piloting layer MPC which then tracks these optimized trajectories. Given the relatively slow thermal dynamics of the cabin, a long prediction horizon is required for energy efficient control of cabin temperature. Consequently, the scheduling layer MPC is formulated over a long prediction horizon (H_l). On the other hand, to reduce the computation burden, the piloting layer MPC is designed with a shorter prediction horizon (H_s) than the scheduling layer MPC. Moreover, the design of the piloting layer MPC can be simplified compared to (18), as the long horizon vehicle speed preview and system constraints are being included and handled at the scheduling layer MPC. The update rates of the two layers are the same in our current implementation (5 s).

A. Scheduling Layer MPC With Long Horizon

The cost function of the scheduling layer MPC is based on several modifications of (18). In order to incorporate the future vehicle speed preview information into the AC MPC, a new variable, η_{AC} , is introduced to bring the sensitivity of the AC system to vehicle speed into the optimization problem formulation. Namely, the cost function associated with the AC system power consumption is defined as

$$\ell_{\text{power}}(i|k) = \frac{P_{\text{comp}}(i|k)}{\eta_{\text{AC}}(i|k)} + P_{\text{bl}}(i|k) \quad (19)$$

where P_{comp} and P_{bl} are calculated according to (4) and (5), respectively. η_{AC} in (19) is dependent on the vehicle speed forecast from the traffic data. When $V_{\text{veh}} = 0$, $\eta_{\text{AC}} = 1$. Once V_{veh} increases, η_{AC} will increase to reflect the increase in the AC system efficiency at higher speeds.

Another term is incorporated in the running cost function of the scheduling layer AC MPC to reflect the objective of maintaining average cabin temperature at the setpoint ($T_{\text{cab}}^{\text{s.p.}}$)

$$\ell_{\text{s.p.}}(i|k) = \left(T_{\text{cab}}^{\text{s.p.}} - \frac{\sum_{i=0}^{H_l} T_{\text{cab}}(i|k)}{H_l + 1} \right)^2 \quad (20)$$

where $\sum_{i=0}^{H_l} T_{\text{cab}}(i|k)/(H_l + 1)$ is the average cabin temperature over the long prediction horizon H_l .

According to (19), the energy-efficient operation of the AC system is achieved if the upper limit of the cabin air temperature $T_{\text{cab}}^{\text{UL}}$ is tracked by the controller. On the other hand, according to (20), the ideal case for the passenger comfort is to perfectly track the commanded temperature setpoint $T_{\text{cab}}^{\text{s.p.}}$. In order to leverage the AC system sensitivity to the vehicle speed for improving the energy efficiency, it is beneficial to follow $T_{\text{cab}}^{\text{UL}}$ during the vehicle stops and put more effort to track $T_{\text{cab}}^{\text{s.p.}}$ during the high-efficiency periods of the AC system operation, i.e., high vehicle speeds. To accomplish this, a third term is added to the running cost, which is referred to as the IOCH term (ℓ_{IOCH})

$$\ell_{\text{IOCH}}(i|k) = \frac{\eta_{\text{AC}}(i|k) - 1}{\epsilon(i|k) + \zeta} \quad (21)$$

where $\zeta > 0$ is a constant. The variable ϵ is a new “slack” (synthetic) optimization variable, which is also used to update

the upper limit of the cabin temperature comfort zone (T_{cab}^{UL}) as follows:

$$\tilde{T}_{cab}^{UL}(i|k) = T_{cab}^{UL}(i) - \epsilon(i|k). \quad (22)$$

ℓ_{IOCH} defined in (22) and the introduction of the slack variable lead to the following properties:

- 1) when $V_{veh} = 0$ and $\eta_{AC} = 1$, $\ell_{IOCH} = 0$;
- 2) when $V_{veh} \rightarrow 0$, $\epsilon \rightarrow 0$, and $T_{cab} \rightarrow T_{cab}^{UL}$;
- 3) when $\eta_{AC} > 1$, \tilde{T}_{cab}^{UL} is decreased to make the AC system work harder (i.e., increase AC load) when the AC system efficiency is higher.

Based on the above-mentioned modifications, the scheduling layer AC MPC with vehicle speed preview incorporated and IOCH mechanism exploits the solution of the following optimization problem:

$$\begin{aligned} & \arg \min_{\substack{T_{evap}^{s.p.}(\cdot|k) \\ W_{bl}(\cdot|k) \\ \epsilon(\cdot|k)}} \sum_{i=0}^{H_l} \ell_{power}(i|k) + \beta \ell_{IOCH}(i|k) + \lambda \ell_{s.p.}(i|k) \\ \text{s.t. } & T_{cab}(i+1|k) = f_{T_{cab}}(i|k), \quad i = 0, \dots, H_l \\ & T_{evap}(i+1|k) = f_{T_{evap}}(i|k), \quad i = 0, \dots, H_l \\ & T_{cab}^{LL} \leq T_{cab}(i|k) \leq T_{cab}^{UL} - \epsilon(i|k), \quad i = 0, \dots, H_l \\ & T_{evap}^{LL} \leq T_{evap}(i|k) \leq T_{evap}^{UL}, \quad i = 0, \dots, H_l \\ & 0.05 \text{ kg/s} \leq W_{bl}(i|k) \leq 0.15 \text{ kg/s}, \quad i = 0, \dots, H_l - 1 \\ & 3 \text{ }^\circ\text{C} \leq T_{evap}^{s.p.}(i|k) \leq 10 \text{ }^\circ\text{C}, \quad i = 0, \dots, H_l - 1 \\ & 0 \text{ }^\circ\text{C} \leq \epsilon(i|k) \leq 3 \text{ }^\circ\text{C}, \quad i = 0, \dots, H_l - 1 \\ & T_{cab}(0|k) = T_{cab}(k), \quad T_{evap}(0|k) = T_{evap}(k). \end{aligned} \quad (23)$$

where β , λ , and ξ are the constant parameters to adjust the tradeoff between AC system energy consumption and cabin temperature setpoint tracking.

B. Piloting Layer MPC With Short Horizon

The planned trajectory of $\tilde{T}_{cab}^{UL}(i|k) = T_{cab}^{UL} - \epsilon(i|k)$ from the scheduling layer MPC is next passed on to the piloting layer MPC, which is designed to track the scheduled trajectories. The piloting layer MPC is defined based on the solution of the following problem over a short horizon (H_s):

$$\begin{aligned} & \arg \min_{\substack{T_{evap}^{s.p.}(\cdot|k) \\ W_{bl}(\cdot|k)}} \sum_{i=0}^{H_s} \left\{ P_{comp}(i|k) + P_{bl}(i|k) \right. \\ & \quad \left. + w_c \left(T_{cab}(i|k) - (T_{cab}^{UL}(i) - \epsilon(i|k)) \right)^2 \right\} \\ \text{s.t. } & T_{cab}(i+1|k) = f_{T_{cab}}(i|k), \quad i = 0, \dots, H_s \\ & T_{evap}(i+1|k) = f_{T_{evap}}(i|k), \quad i = 0, \dots, H_s \\ & 0.05 \text{ kg/s} \leq W_{bl}(i|k) \leq 0.15 \text{ kg/s}, \quad i = 0, \dots, H_s - 1 \\ & 3 \text{ }^\circ\text{C} \leq T_{evap}^{s.p.}(i|k) \leq 10 \text{ }^\circ\text{C}, \quad i = 0, \dots, H_s - 1 \\ & T_{cab}(0|k) = T_{cab}(k), \quad T_{evap}(0|k) = T_{evap}(k). \end{aligned} \quad (24)$$

Compared to the scheduling layer MPC (23), the piloting layer MPC has fewer optimization variables and constraints, a less complicated cost function, and a shorter prediction horizon ($H_l > H_s$). To reduce the fluctuation of the piloting layer MPC setpoint (\tilde{T}_{cab}^{UL}), the optimized values of ϵ from the scheduling layer MPC are quantized before being passed on

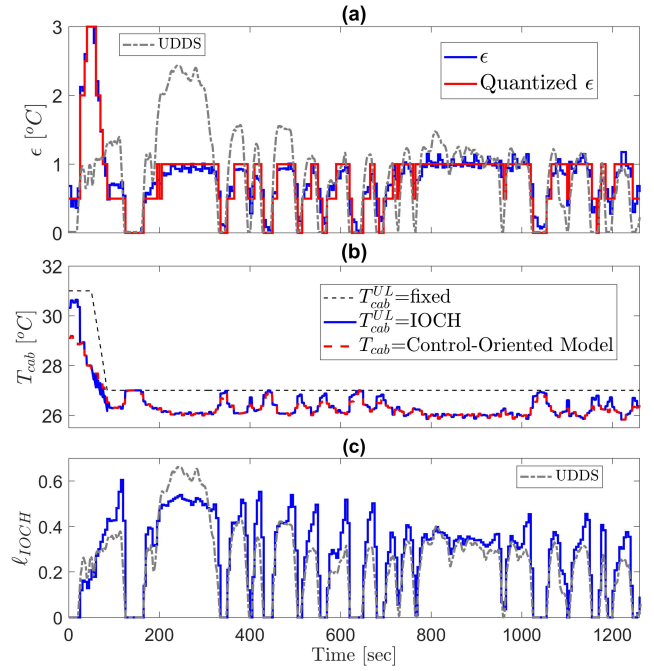


Fig. 8. IOCH performance for the UDDS. (a) Calculated ϵ from scheduling layer MPC and the quantized ϵ passed on to the piloting layer MPC. Gray curve: scaled vehicle speed over UDDS. (b) Cabin temperature from the control-oriented model and the updated T_{cab}^{UL} via the IOCH. (c) IOCH cost function (ℓ_{IOCH}) against the vehicle speed profile.

to the piloting layer MPC. Specifically, in our implementation, ϵ is quantized with a quantization step of 0.5 °C. This approach is preferred to adding a rate penalty to (23), as it still enables $\epsilon(i|k)$ to respond rapidly when there are fast changes in vehicle speed and hence in AC system efficiency.

Fig. 8 shows the results of implementing the AC MPC based on (23) and piloting layer MPC (24) on the control-oriented model, i.e., the same model used for prediction. In the simulations, the horizon of scheduling layer MPC is $H_l = 12$ (60 s) and of the piloting layer $H_s = 6$ (30 s). Perfect time-varying vehicle speed preview is assumed over the horizon in the scheduling and piloting layer MPCs. The calculated $\epsilon(k)$ along with the time history of the vehicle speed over UDDS is plotted in Fig. 8(a). As expected $\epsilon(k)$ decreases to zero whenever V_{veh} decreases to zero. As can be observed in Fig. 8(b), T_{cab} follows $\tilde{T}_{cab}^{UL} = T_{cab}^{UL} - \epsilon$, which exhibits the desired energy efficient cooling profile. Furthermore, Fig. 8(c) verifies that the desirable response of ℓ_{IOCH} as a function of the vehicle speed (i.e., $\ell_{IOCH}(k)$ decreases to zero when $V_{veh}(k)$ decreases to zero).

Fig. 8(a) shows the actual $\epsilon(k) = \epsilon(0|k)$ and the quantized $\epsilon(k)$, which is passed on to the piloting layer MPC in these simulations. In addition to the AC MPC, the MPC for battery temperature control from (17) is implemented with $N_1 = H_s$ (decentralized from AC MPC). Fig. 9 shows the overall schematic of the optimization-based battery and cabin thermal management using a two-layer MPC with IOCH. While the hierarchical framework shown in Fig. 9 is generic and it allows for incorporation of weather forecast information, in this paper, we assume that the ambient temperature and weather conditions are constant.

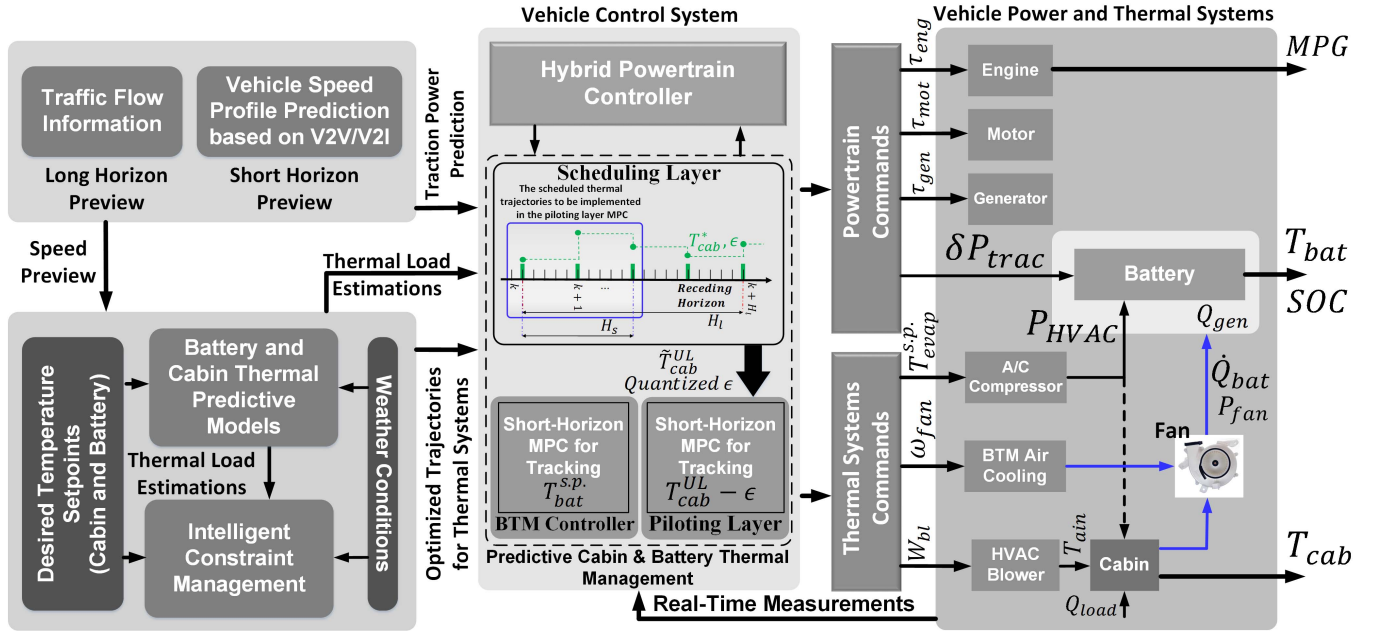


Fig. 9. Overall schematic of the optimization-based battery and cabin thermal management system integrated with traffic and V2X information for HEVs. While the thermal system commands ($T_{evap}^{s.p.}$, W_{bl} , and ω_{fan}) are determined by the AC and BTM MPCs, the powertrain commands [engine torque (τ_{eng}), motor torque (τ_{mot}), and generator torque (τ_{gen})] are calculated by the HEV power-split controller.

C. Simulation Results of Two-Layer MPC on High-Fidelity CoolSim Model

In this section, different characteristics of the proposed two-layer AC MPC that attribute to battery energy saving are illustrated and further discussed in what follows informing further controller evolution with the CSOL. High-fidelity CoolSim models for the AC system and the experimentally validated battery thermal model (6) are used as virtual testbed to implement and evaluate the performance of the proposed two-layer MPC.

1) *AC Load Optimization and Shift via IOCH Mechanism:* Fig. 10 presents the results of implementing the two-layer MPC for cabin thermal management and the decentralized MPC for BTM over UDSS on the high-fidelity thermal simulation models. For the hierarchical MPC in (23) and (24), the sampling time of $T = 5$ s is used for both layers. Moreover, $N_1 = H_s = 6$ (30 s) and $H_l = 12$ (60 s). The driver/passenger requests $T_{cab}^{s.p.} = 26$ °C. Assuming $SOC(0) = 95\%$, it can be observed that the single-layer AC MPC (18) consumes a considerable part of the battery energy [Fig. 10(d)] for tracking $T_{cab}^{s.p.}$. On the other hand, according to the vehicle speed profile, the two-layer MPC schedules \tilde{T}_{bat}^{UL} to reduce the load on the AC compressor when V_{veh} decreases to zero [Fig. 10(a)]. In other words, the IOCH mechanism (21) allows for shifting the AC load from the inefficient periods, i.e., vehicle stops, to the high-efficiency periods, i.e., high vehicle speeds. As shown in Fig. 10(d), the two-layer MPC is able to save 5.4% of the battery energy, as compared to the single-layer AC MPC (for tracking constant $T_{cab}^{s.p.}$), by taking proactive actions to minimize the cooling load on the AC compressor during low-efficiency periods of the AC system operation.

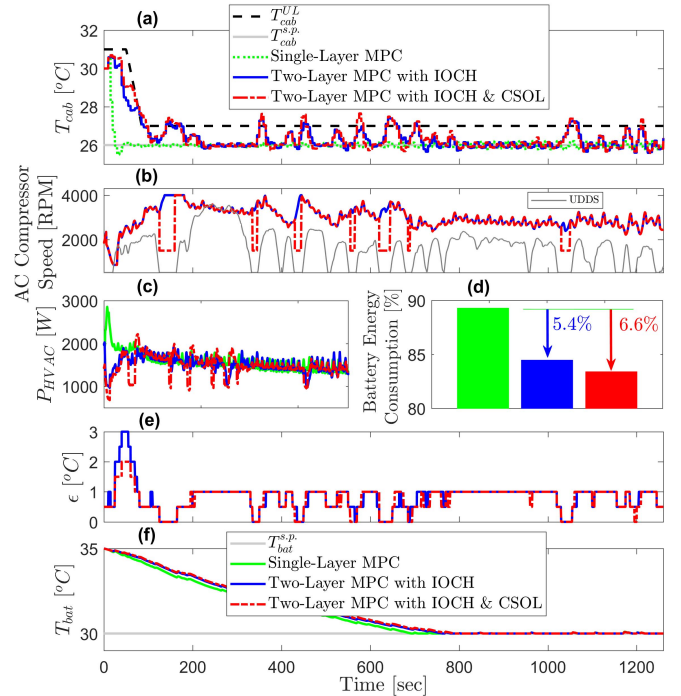


Fig. 10. Overall performance of the two-layer MPC with IOCH mechanism for constant $T_{cab}^{s.p.}$ and UDSS. (a) T_{cab} . (b) AC compressor speed for two-layer MPC with IOCH and two-layer MPC with IOCH and CSOL. (c) AC compressor power consumption. (d) Battery energy consumption. (e) Quantized ϵ calculated at the scheduling layer MPC. (f) Battery temperature.

The plotted results in Fig. 10(a) show an average cabin temperature of 26 °C for the single-layer MPC, compared to the value of 26.5 °C for the two-layer MPC with IOCH.

This means that 5.4% of the battery energy can be saved by allowing the average cabin temperature to slightly rise. Fig. 10(b), (c), and (e) shows the compressor speed, AC power demand ($P_{\text{comp}} + P_{\text{bl}}$) and the quantized ϵ calculated by the scheduling layer MPC. Moreover, the performance of the BTM MPC for tracking $T_{\text{bat}}^{\text{s.p.}}$ is shown in Fig. 10(f). Since the single-layer MPC cools the cabin faster and T_{cab} is slightly lower on average, the resulting average T_{bat} is slightly lower than in the case of the two-layer MPC. It should be noted that a lower T_{cab} does not necessarily lead to better BTM, as lowering T_{cab} requires higher AC compressor power consumption, which means more current being drawn from the battery and more heat is generated.

2) *Cabin Air as a Thermal Storage*: The relatively slow dynamics of the cabin air temperatures provide a unique opportunity to treat the cabin air as a “temporary” thermal storage. When a long stop duration is projected by the scheduling layer MPC along the prediction horizon, the controller plans to reduce the load on the AC compressor. This means that when the vehicle comes to a complete stop, T_{cab} starts to rise as, for example, is visible in Fig. 10(a) between 150 and 200 s. However, due to the slow dynamics of T_{cab} , it does not rise immediately, and it takes a while until T_{cab} reaches $T_{\text{cab}}^{\text{UL}}$. Thus, energy can be saved by shutting off the compressor. When the vehicle starts to move again after a temporary stop, the AC compressor can start to run to compensate for the rise in the cabin temperature.

3) *Compressor Shutoff Logic*: In order to take advantage of the available “temporary” thermal storage within the cabin and further increase energy savings, we incorporate an add-on CSOL into the piloting layer MPC. Note that if the compressor is completely turned off during the vehicle stop period, T_{cab} may increase to even above $T_{\text{cab}}^{\text{UL}}$, which may be unacceptable to customers. Moreover, recovering the cabin temperature from beyond $T_{\text{cab}}^{\text{UL}}$ to the comfort zone will increase the cooling load significantly. Thus, to minimize $T_{\text{cab}}^{\text{UL}}$ constraint violation and avoid imposing unexpected cooling load on the AC compressor, instead of completely turning the compressor off, the CSOL is introduced to reduce the compressor speed to below 2000 r/min when the following conditions hold:

- 1) $\epsilon(1|k) = \epsilon(2|k) = 0$;
- 2) $T_{\text{cab}}(k) < T_{\text{cab}}^{\text{UL}}(k) + \vartheta$, $1 > \vartheta > 0$ °C.

The first criterion implies that CSOL could reduce the compressor speed if the vehicle is expected to come to a complete stop for at least 10 s. This condition is imposed to ignore nonsignificant vehicle stop events and minimize the transients in the compressor operation. The second condition ensures that T_{cab} will not increase above $T_{\text{cab}}^{\text{UL}} + \vartheta$ as a result of CSOL, where ϑ is a small number (e.g., 0.5 °C).

The responses with the two-layer MPC and the CSOL are also plotted in Fig. 10. It can be seen in Fig. 10(a) that when CSOL conditions are fulfilled, T_{cab} increases slightly above $T_{\text{cab}}^{\text{UL}}$. At the same time, CSOL decreases the compressor speed [Fig. 10(b)] at vehicle stops, which, consequently, reduces the AC system power consumption [Fig. 10(c)]. As shown in Fig. 10(d), the two-layer MPC equipped with IOCH and CSOL is able to save 6.6% of the battery energy

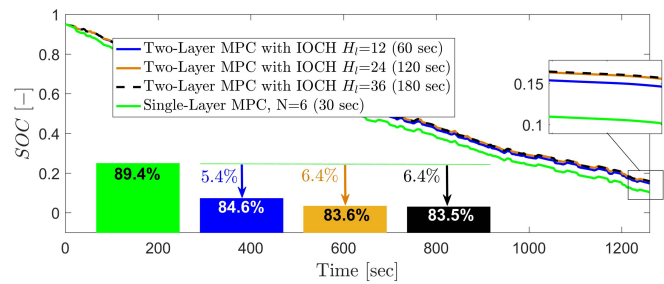


Fig. 11. Effect of increasing the scheduling layer MPC prediction horizon (H_1) of the two-layer MPC on the battery energy consumption for UDDS. $N_1 = H_s = 6$ (30 s).

at the end of the driving cycle, compared to the single-layer MPC.

4) *Impact of the Prediction Horizon (H_1) Length*: The results shown in Fig. 10 are based on a scheduling MPC layer with $H_1 = 12$ (60 s). Fig. 11 shows that by increasing H_1 from 12 to 36 (180 s), the energy saving potential of the two-layer MPC with vehicle speed preview and IOCH mechanism will increase from 5.4% to 6.4%. This is expected as increasing the prediction horizon makes more information available to the controller, and the output of the scheduling layer MPC is closer to the global optimal solution. However, there are two issues that complicate the implementation of the scheduling layer MPC with a long horizon. First, the prediction of future vehicle speed profile over a long horizon (e.g., greater than 30 s) may not be reliable. Second, extending the prediction horizon may significantly increase the MPC computation effort, thereby making the real-time implementation of the controller more difficult. Section V addresses these issues.

V. INTEGRATING TRAFFIC FLOW MODEL FOR LONG HORIZON PREDICTION

As discussed in Section IV (Fig. 11), the information about future driving conditions, in particular, the vehicle speed profile over a long horizon, can facilitate the design of an energy-efficient AC system. In this section, we highlight the opportunity to base an approximate knowledge of future vehicle speed profile on the average traffic flow velocity estimate (V_{flow}) following the approach proposed in [28]. This knowledge, when integrated into the two-layer MPC controller, can reduce energy consumption. While the knowledge of the exact demanded traction power over a short horizon is essential for the energy management of the HEVs, it will be shown, in this section, that even a very approximate knowledge of the traffic flow information over a long horizon can be beneficial for the cabin and BTM.

In [28], the traffic flow data are extracted from a traffic monitoring system described in [32], based on GPS-enabled smartphones. This system exploits the extensive coverage of the cellular network, GPS-based position and velocity measurements, and the communication infrastructure of cell-phones. In [28], the traffic speed is calculated according to the moving average of the recorded speed trajectories of 100 vehicles traveling following the same route as the “host” vehicle over a moving time-window of 120–180 s.

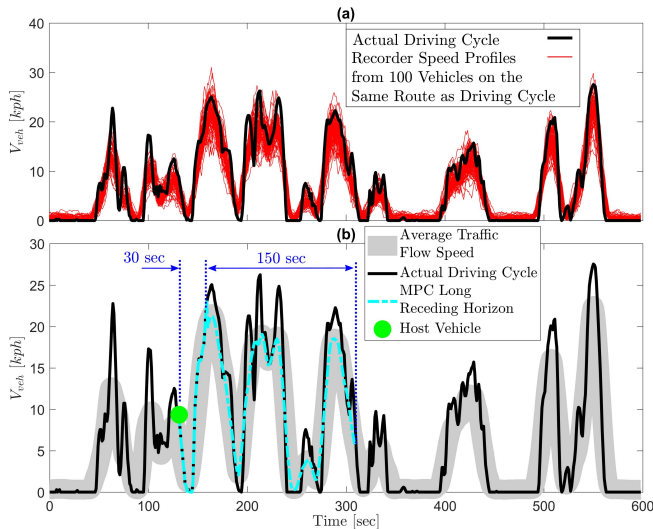


Fig. 12. Average traffic flow speed estimate versus the actual speed over a driving cycle.

Not all of these vehicles are required to be on the same route as the host vehicle for the entire simulation time, instead the speed signals of the vehicles exiting the route are replaced by those entering the route, so that the traffic flow speed is estimated based on a large set of vehicles speed trajectories along the host vehicle route. With this approach, it is possible to build a dynamic map of average traffic velocity over a long horizon.

In this paper, we assume that the vehicle speed can be accurately estimated over a 30-s horizon on-board of CAV using vehicle and V2V/V2I information [33], while for the rest of the long horizon, the average traffic flow information is used to forecast the vehicle speed and resulting thermal loads. It is envisioned that the traffic flow data are being collected, analyzed, and updated by a central/cloud server in real-time, and they are available to the vehicle control system at no extra computational cost. In addition, V_{flow} is updated every 5 s as the traffic flow changes downstream. Fig. 12 illustrates the concept of the average traffic flow speed trajectory and compares it against the actual speed profile. As can be observed in Fig. 12(b), over the long receding horizon of the MPC, the vehicle speed is accurately predicted for the first 30 s. Then, the predicted vehicle speed merges into the average traffic flow speed band [the gray band in Fig. 12(b)] over the long horizon.

Fig. 13 shows the results of testing the two-layer MPC with exact vehicle speed profile and estimated traffic flow speed information (Fig. 12) over the long prediction horizon. It was previously shown in Fig. 11 that increasing H_l from 24 to 36 does not considerably improve the energy saving results. Thus, to keep the computation time of the scheduling layer MPC as low as possible, the value of $H_l = 24$ (corresponding to a 120-s time window) is selected. Compared with the two-layer MPC with exact vehicle speed profile, it is observed that the two-layer MPC with exact vehicle speed profile and traffic flow information results in a similar cabin thermal management [Fig. 13(a)] and that the energy saving results

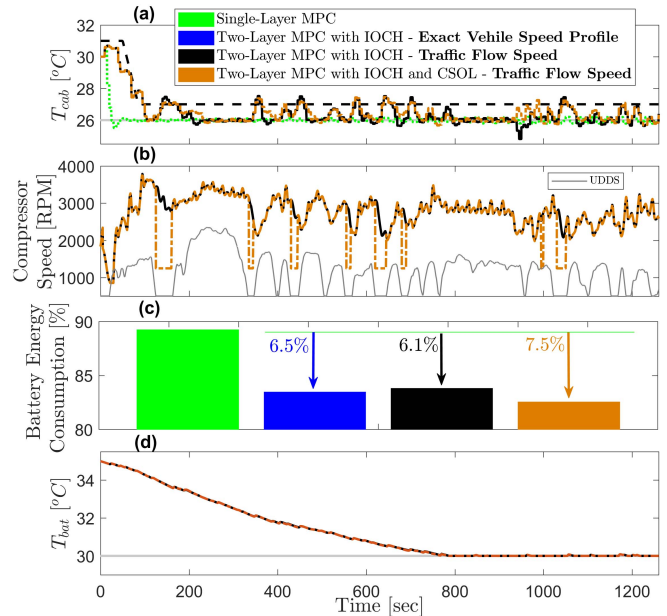


Fig. 13. Overall performance of the two-layer MPC with IOCH mechanism with exact vehicle speed profile and with traffic flow speed information for the UDDS. (a) T_{cab} . (b) AC compressor speed for two-layer MPC with IOCH and two-layer MPC with IOCH and CSOL. (c) Battery energy consumption. (d) Battery temperature. $N_1 = H_s = 6$ (30 s) and $H_l = 24$ (120 s).

from the two-layer MPC with traffic flow information are still substantial (6.1% less battery energy consumed compared with the single-layer MPC). Furthermore, by inclusion of the CSOL in the two-layer MPC solution, the battery energy saving from the predictive controller with estimated vehicle speed from average traffic flow information over the long horizon is increased to 7.5%. Eventually, Fig. 13(d) shows that the BTM results are similar for all studied cases, as the cabin temperature is the same. This is mainly due to the relatively slow dynamics of the cabin temperature. Consequently, only significant changes in vehicle speed along the driving route affect the thermal system behavior, and the proposed approach to traffic speed estimation is able to reflect these changes sufficient accurately for the thermal management purposes.

A. Performance Evaluation in Congested Driving Scenario

In this section, the performance of the two-layer MPC for cabin and BTM is evaluated for congested driving over the NYCC, which features low speed stop-and-go traffic conditions. Compared with UDDS, NYCC has longer stop periods and the maximum vehicle speed is lower (< 12 m/s). This means that the vehicle does not reach the high AC system efficiency region (Fig. 7) at high speeds (> 20 m/s). However, due to long stop periods, and variations in the AC system efficiency even at lower speeds, it is still beneficial to incorporate the long horizon preview into the two-layer MPC to optimize the AC cooling load.

Fig. 14 shows the performance of the two-layer MPC with IOCH and long horizon preview based on the traffic flow information for NYCC. The host vehicle has a long stop at the beginning of NYCC for about 50 s. During this period, since

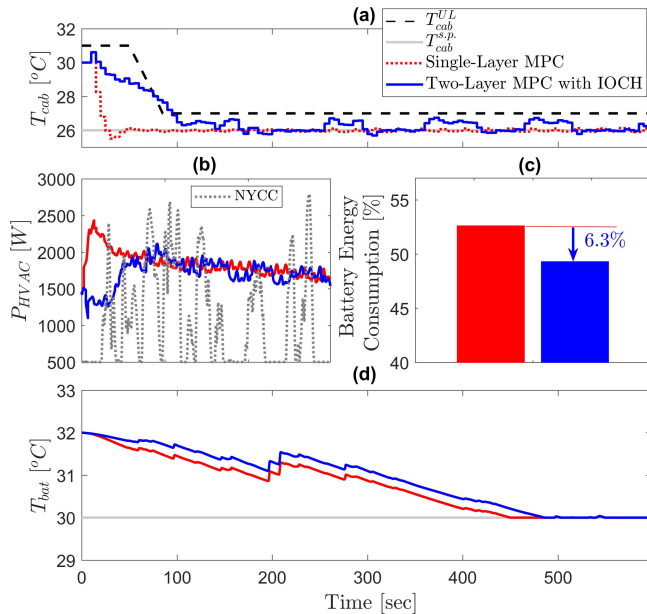


Fig. 14. Overall performance of the two-layer MPC with IOCH mechanism with traffic flow speed information for the NYCC. (a) T_{cab} . (b) P_{HVAC} . (c) Battery energy consumption. (d) Battery temperature. $N_1 = H_s = 6$ (30 s) and $H_l = 24$ (120 s).

the cabin air initial temperature is high (30 °C), the single-layer MPC based on (18) puts all the effort to cool the cabin immediately. On the other hand, the two-layer MPC detects this long stop according to the traffic flow data and relaxes the initial cabin cooling by enforcing T_{cab} to be within the comfort zone [Fig. 14(a)], while the AC cooling load is minimized [Fig. 14(b)] to account for the inefficiency of the AC system during this period. Similarly, for the other major vehicle stops along the driving cycle, the two-layer MPC reduces the AC cooling load accordingly. Eventually, Fig. 14(c) shows that by taking the proactive actions suggested by the two-layer MPC, up to 6.3% of the battery energy can be saved compared to the single-layer MPC. By the end of the driving cycle, T_{cab} is 2.3% higher on average by using the two-layer MPC compared to the single-layer MPC. Moreover, with $T_{bat}(0) = 32$ °C, it can be observed in Fig. 14(d) that the average T_{bat} is slightly higher (< 1 °C) for the two-layer MPC; however, both controllers eventually steer T_{bat} to the desired setpoint $T_{bat}^{S.P.}$.

B. Real-Time Implementation of the Hierarchical AC MPC

In order to demonstrate the feasibility capability of the proposed two-layer hierarchical MPC solution for the AC system, the controller is implemented on a Speedgoat rapid prototyping system with an Intel Celeron Core i4@2.0 GHz processor. The controller is run in closed loop with the control-oriented AC model, which is sufficient, as the primary purpose is the evaluation of the controller computational footprint. The MPC is implemented in MATLAB/SIMULINK using C-code based S-functions, and the sequential quadratic programming algorithm [34] with Fischer Burmeister regularized smoothed quadratic programming solver [35] has been used for solving the optimization problem numerically.

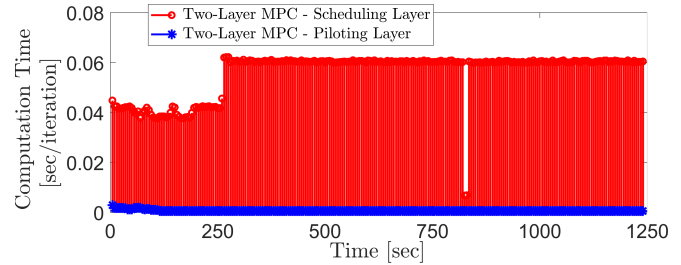


Fig. 15. Real-time computation times of the scheduling and piloting layers MPC over UDSS with $H_s = 6$ (30 s) and $H_l = 24$ (120 s) implemented on the Speedgoat.

The computation times incurred at the scheduling, and piloting layers over UDSS are plotted in Fig. 15. The update rates of both MPCs are 5 s. As shown in Fig. 15, the piloting layer MPC with a short prediction horizon of $H_s = 6$ requires on average 0.558 ms for the computations, with maximum computation time of 2.9 ms. At the same time, the scheduling layer MPC requires longer computation times, as it has more optimization variables and constraints with longer prediction horizon. The results in Fig. 15 show that the scheduling layer MPC with $H_l = 24$ requires an average computation time of 55.829 ms. The scheduling and piloting layer MPCs run simultaneously, thereby the overall computation time of the two-layer MPC is dictated by the slower layer (scheduling layer) with the maximum computation time of up to 62 ms. It can be observed that the computation times of the piloting and scheduling layer MPCs are well below the time available to perform the updates (5000 ms), thereby confirming the feasibility of implementing the hierarchical MPC in real-time. While the capability of the Speedgoat rapid prototyping system exceeds the capability of ECUs used in conventional vehicles, larger computing power is typically assumed to be available on-board of CAVs, which would be on par and exceed that of Speedgoat rapid prototyping system. Furthermore, since only about a 1/100 fraction of Speedgoat computing capability is needed, the implementation in less capable processors is also likely to be feasible.

VI. VEHICLE-LEVEL IMPLEMENTATION OF THE TWO-LAYER MPC WITH IOCH

The results presented in Section IV and V were based on the assumption that the demanded fraction of the traction power from the battery (δP_{trac}) and hence the demanded fraction of the traction power from the ICE are the same for all scenarios. In this section, this assumption is relaxed and the developed two-layer MPC from Section IV is implemented at the vehicle level with the hybrid controller of the Prius HEV simulation model, which also includes a power split logic adopted from Autonomie software [26]. The power split logic sustains the battery charge by the end of the driving cycle so that $SOC(0) = SOC(k_f)$. Fig. 16(a) shows that charge sustainability constraint is met over the UDSS for both single-layer and two-layer controllers. However, since the two-layer MPC consumes less battery energy for thermal management, SOC is higher on average for the two-layer MPC compared to

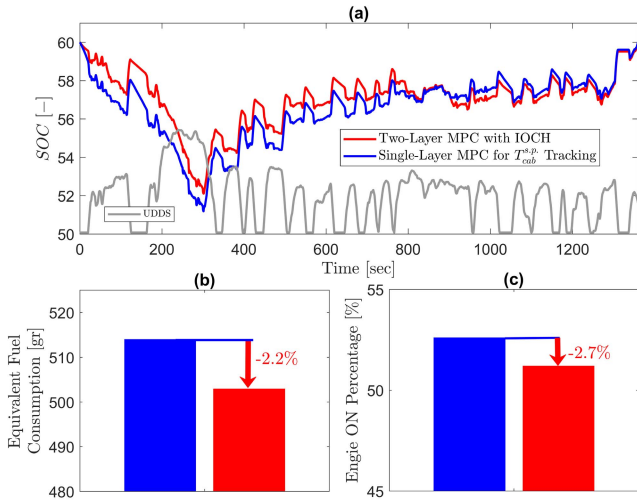


Fig. 16. Results of implementing the single-layer and two-layer MPC with IOCH mechanisms on the high-fidelity Autonomie HEV model for overall fuel consumption evaluation over UDDS assuming $SOC(0) = 60\%$. (a) SOC. (b) Equivalent fuel consumption. (c) Combustion engine on-percentage. $N_1 = H_s = 6$ (30 s) and $H_l = 24$ (120 s).

the single-layer MPC. This means that the power-split logic commands the ICE to run for a longer time to compensate the drop in SOC from the single-layer MPC so that the battery charge is sustained by the end of the driving cycle. Consequently, the overall fuel consumption is higher for the single-layer MPC. As shown in Fig. 16(b), the two-layer MPC reduces the HEV equivalent fuel consumption by 2.2% while reducing the engine on-percentage by 2.7% during the driving cycle. This improvement is attributed to the inclusion of future vehicle speed prediction into the optimization.

For the congested city driving cycle (e.g., NYCC), as shown in Fig. 17, the two-layer MPC with IOCH is able to reduce the HEV fuel consumption by 5.3%, compared to the single-layer MPC that tracks a constant cabin temperature setpoint (Fig. 14). Compared to the single-layer MPC, the two-layer MPC decreases the fuel consumption by reducing the AC cooling load on the battery at relatively long vehicle stops over the congested driving cycle, which results in less battery charge depletion. Consequently, the ICE needs to run for a shorter time by 6.7% [Fig. 17(c)]. By comparing UDDS and NYCC results shown in Figs. 16 and 17, it can be observed that the energy saving resulted from two-layer MPC is larger for NYCC. This is attributed to the cumulative vehicle stop time being longer on NYCC than on UDDS. Thus, if the AC cooling load is not optimized with respect to traffic conditions and the AC compressor keeps working during the long stops, the battery charge will drop quickly. Moreover, compared to UDDS, the average traction power is lowered by 70% for the congested traffic condition over NYCC. Assuming the same weather and initial cabin temperature conditions, the AC system power consumption is in the same range for both driving cycles. Therefore, the ratio of AC cooling power to the NYCC traction power is much higher than the same ratio for UDDS, meaning that the optimization of the AC cooling load will have a more significant impact on the fuel consumption rate for the congested driving cycle, as shown in Fig. 17.

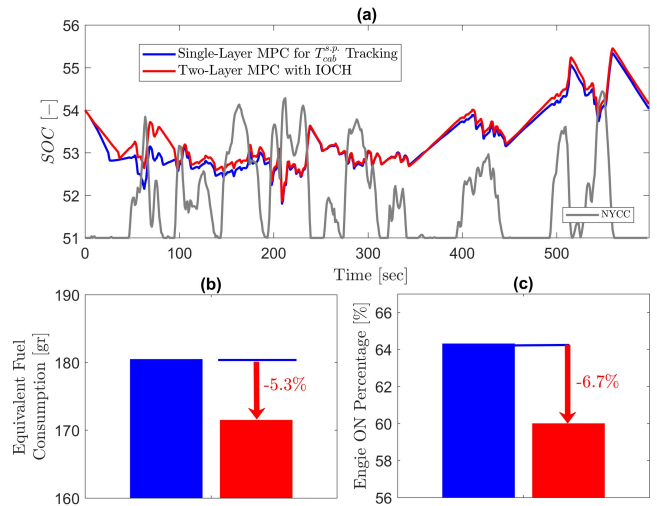


Fig. 17. Results of implementing the single-layer and two-layer MPC with IOCH mechanism on the high-fidelity Autonomie HEV model for overall fuel consumption evaluation over NYCC assuming $SOC(0) = 54\%$. (a) SOC. (b) Equivalent fuel consumption. (c) Combustion engine on-percentage. $N_1 = H_s = 6$ (30 s) and $H_l = 24$ (120 s).

VII. CONCLUSION

A hierarchical MPC-based cabin and BTM strategy has been developed in this paper to improve energy efficiency of HEVs. Our approach also exploits novel opportunities emerging with broadening use of CAV technologies. The proposed hierarchical MPC framework could be useful for other systems that have multiple time-scales with slow (storage) states and that need to integrate the preview. In the case considered in this paper, the optimization of the cabin thermal system operation with slow dynamics requires a relatively long planning horizon to achieve near-optimal performance. The two-layer MPC with the scheduling and piloting layers employing different horizons, costs, and constraints provides necessary flexibility to accommodate the long horizon preview into the dynamic optimization at a manageable computational cost. The fuel economy improvements demonstrated in this paper are attributed to the two-layer MPC solution being able to exploit the AC system sensitivity to vehicle speed, treating the cabin air as a thermal storage, and CSOL, while maintaining the comfort at the same level.

The simulation results of implementing the two-layer MPC on the high-fidelity CoolSim and Autonomie simulation models showed the following.

- 1) For the urban driving cycle (UDDS), up to 6.1% of the battery energy can be saved with a two-layer MPC as compared to a more traditional single-layer MPC solution while the passenger comfort is not affected. It was shown that further energy saving up to 7.5% can be achieved by inclusion of an add-on logic (CSOL) to reduce the AC compressor load during long vehicle stops.
- 2) While long prediction horizon with exact vehicle speed profile preview is needed to achieve maximum energy saving, even an inaccurate estimate of the future traffic speed, which captures major traffic events affecting

TABLE I
MODEL PARAMETERS

$m_{bat} = 1.0200$ [kg/module]	$C_{th,bat} = 521$ [J/KgK]
$m = 1450$ [kg]	$A_f = 2.52$ [m ²]
$C_d = 0.28$ [-]	$\rho = 1.2$ [kg/m ³]
$C_r = 0.015$ [-]	$C_{nom} = 3600$ [Wh]

the vehicle thermal system over the longer prediction horizon, can still be used to substantially improve the efficiency of the thermal management system.

- 3) At the vehicle level, with a power split control enforcing the battery charge sustaining constraint, the HEV fuel consumption is reduced by 2.2% over UDDS by a two-layer MPC as compared to the single-layer MPC, representing a more traditional approach for thermal management. For low-speed congested driving cycles, e.g., NYCC, where the ratio of power consumed for thermal management to the traction power is more significant, the two-layer MPC showed a reduction of 5.3% in the vehicle fuel consumption, compared to the single-layer MPC, by taking proactive actions to avoid unnecessary cooling loads with respect to the average traffic flow information.

Finally, the two-layer MPC has been implemented in a Speedgoat rapid prototyping system, and the feasibility of performing the required computations in real-time has been demonstrated.

While the robustness of the proposed hierarchical AC MPC against the traffic prediction uncertainties was studied and confirmed, a comprehensive study of robustness to other noise factors, including opportunities to improve robustness through design changes or taking advantage of connectivity (e.g., to a weather station that provides humidity information), is left as the topic for future research.

APPENDIX

See Table I.

REFERENCES

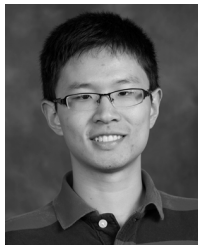
- [1] M. A. Jeffers, L. Chaney, and J. P. Rugh, "Climate control load reduction strategies for electric drive vehicles in warm weather," SAE Tech. Paper 2015-01-0355, 2015.
- [2] J. Rugh and R. Farrington, "Vehicle ancillary load reduction project close-out report: An overview of the task and a compilation of the research results," Nat. Renew. Energy Lab., Golden, CO, USA, Tech. Rep. NREL/TP-540-42454, 2008.
- [3] A. Vahidi and A. Sciarretta, "Energy saving potentials of connected and automated vehicles," *Transp. Res. C, Emerg. Technol.*, vol. 95, pp. 822–843, Oct. 2018.
- [4] J. Guanetti, Y. Kim, and F. Borrelli, "Control of connected and automated vehicles: State of the art and future challenges," *Annu. Rev. Control*, vol. 45, pp. 18–40, May 2018.
- [5] C. Rostiti, S. Stockar, and M. Canova, "A rule-based control for fuel-efficient automotive air conditioning systems," SAE Tech. Paper 2015-01-0366, 2015.
- [6] Q. Zhang and M. Canova, "Modeling air conditioning system with storage evaporator for vehicle energy management," *Appl. Therm. Eng.*, vol. 87, pp. 779–787, Aug. 2015.
- [7] H. Wang, I. Kolmanovsky, M. R. Amini, and J. Sun, "Model predictive climate control of connected and automated vehicles for improved energy efficiency," in *Proc. Amer. Control Conf.*, Milwaukee, WI, USA, 2018.
- [8] M. R. Amini, X. Gong, Y. Feng, H. Wang, I. Kolmanovsky, and J. Sun, "Sequential optimization of speed, thermal load, and power split in connected HEVs," in *Proc. Amer. Control Conf.*, Philadelphia, PA, USA, 2019.
- [9] K. Vatanparvar and M. A. Al Faruque, "Design and analysis of battery-aware automotive climate control for electric vehicles," *ACM Trans. Embedded Comput. Syst.*, vol. 17, no. 4, 2018, Art. no. 74.
- [10] S. Bauer, A. Suchanek, and F. León, "Thermal and energy battery management optimization in electric vehicles using Pontryagin's maximum principle," *J. Power Sources*, vol. 246, pp. 808–818, Jan. 2014.
- [11] Y. Masoudi, A. Mozaffari, and N. L. Azad, "Battery thermal management of electric vehicles: An optimal control approach," in *Proc. ASME Dyn. Syst. Control Conf.*, Columbus, OH, USA, 2015, Art. no. V001T13A003.
- [12] Y. Masoudi and N. L. Azad, "MPC-based battery thermal management controller for plug-in hybrid electric vehicles," in *Proc. Amer. Control Conf.*, Seattle, WA, USA, 2017, pp. 4365–4370.
- [13] X. Tao and J. Wagner, "Cooling air temperature and mass flow rate control for hybrid electric vehicle battery thermal management," in *Proc. ASME Dyn. Syst. Control Conf.*, San Antonio, TX, USA, 2014, Art. no. V002T34A002.
- [14] X. Tao, K. Zhou, A. Ivanco, J. Wagner, H. Hofmann, and Z. Filipi, "A hybrid electric vehicle thermal management system—Nonlinear controller design," SAE Tech. Paper 2015-01-1710, 2015.
- [15] J. Brusey, D. Hintea, E. Gaura, and N. Beloe, "Reinforcement learning-based thermal comfort control for vehicle cabins," *Mechatronics*, vol. 50, pp. 413–421, Apr. 2018.
- [16] S. R. Cominesi, M. Farina, L. Giulioni, B. Picasso, and R. Scattolini, "A two-layer stochastic model predictive control scheme for microgrids," *IEEE Trans. Control Syst. Technol.*, vol. 26, no. 1, pp. 1–13, Jan. 2018.
- [17] W. C. Clarke, C. Manzie, and M. J. Brear, "Hierarchical economic MPC for systems with storage states," *Automatica*, vol. 94, pp. 138–150, Aug. 2018.
- [18] J. P. Koeln and A. G. Alleyne, "Robust hierarchical model predictive control of graph-based power flow systems," *Automatica*, vol. 96, pp. 127–133, Oct. 2018.
- [19] M. Farina, X. Zhang, and R. Scattolini, "A hierarchical multi-rate MPC scheme for interconnected systems," *Automatica*, vol. 90, pp. 38–46, Apr. 2018.
- [20] A. Lefort, R. Bourdais, G. Ansanay-Alex, and H. Guéguen, "Hierarchical control method applied to energy management of a residential house," *Energy Buildings*, vol. 64, pp. 53–61, Sep. 2013.
- [21] T. Kiss, L. Chaney, and J. Meyer, "A new automotive air conditioning system simulation tool developed in MATLAB/simulink," SAE Tech. Paper 2013-01-0850, 2013.
- [22] T. Kiss and J. Lustbader, "Comparison of the accuracy and speed of transient mobile A/C system simulation models: Preprint," *SAE Int. J. Passenger Cars-Mech. Syst.*, vol. 7, no. 2, pp. 739–754, 2014.
- [23] A. Kelman and F. Borrelli, "Bilinear model predictive control of a HVAC system using sequential quadratic programming," in *Proc. 18th IFAC World Congr.*, Milan, Italy, 2011, pp. 9869–9874.
- [24] M. Bhatti, "A critical look at R-744 and R-134a mobile air conditioning systems," SAE Tech. Paper 970527, 1997.
- [25] T. Yuksel and J. Michalek, "Development of a simulation model to analyze the effect of thermal management on battery life," SAE Tech. Paper 2012-01-0671, 2012.
- [26] S. Halbach, P. Sharer, S. Pagerit, A. Rousseau, and C. Folkerts, "Model architecture, methods, and interfaces for efficient math-based design and simulation of automotive control systems," SAE Tech. Paper 2010-01-0241, 2010.
- [27] M. Zolot, A. Pesaran, and M. Mihalic, "Thermal evaluation of toyota prius battery pack," SAE Tech. Paper 2002-01-1962, 2002.
- [28] C. Sun, F. Sun, X. Hu, J. Hedrick, and S. Moura, "Integrating traffic velocity data into predictive energy management of plug-in hybrid electric vehicles," in *Proc. Amer. Control Conf.*, Chicago, IL, USA, 2015, pp. 3267–3272.
- [29] J. Lofberg, "YALMIP: A toolbox for modeling and optimization in MATLAB," in *Proc. IEEE Int. Symp. Comput. Aided Control Sys. Design*, New Orleans, LA, USA, 2004, pp. 284–289.
- [30] A. Wächter and L. T. Biegler, "On the implementation of an interior-point filter line-search algorithm for large-scale nonlinear programming," *Math. Program.*, vol. 106, no. 1, pp. 25–57, 2006.

- [31] M. R. Amini, I. Kolmanovsky, and J. Sun, "Two-layer model predictive battery thermal and energy management optimization for connected and automated electric vehicles," in *Proc. 57th Conf. Decis. Control*, Miami Beach, FL, USA, 2018, pp. 6976–6981.
- [32] J. C. Herrera, D. B. Work, R. Herring, X. (Jeff) Ban, Q. Jacobson, and A. M. Bayen, "Evaluation of traffic data obtained via GPS-enabled mobile phones: The mobile century field experiment," *Transp. Res. C, Emerg. Technol.*, vol. 18, no. 4, pp. 568–583, Aug. 2010.
- [33] D. Moser, H. Waschl, R. Schmied, H. Efendic, and L. del Re, "Short term prediction of a vehicle's velocity trajectory using ITS," *SAE Int. J. Passenger Cars-Electron. Electr. Syst.*, vol. 8, no. 2, pp. 364–370, Apr. 2015.
- [34] M. Diehl, R. Findeisen, F. Allgöwer, H. G. Bock, and J. P. Schlöder, "Nominal stability of real-time iteration scheme for nonlinear model predictive control," *IEE Proc.-Control Theory Appl.*, vol. 152, no. 3, pp. 296–308, 2005.
- [35] D. Liao-McPherson, M. Huang, and I. Kolmanovsky, "A regularized and smoothed fischer–burmeister method for quadratic programming with applications to model predictive control," *IEEE Trans. Autom. Control*, vol. 64, no. 7, pp. 2937–2944, Jul. 2019.



Mohammad Reza Amini received the Ph.D. degree in mechanical engineering from Michigan Technological University, Houghton, MI, USA, in 2017.

He is currently an Assistant Research Scientist with the College of Engineering, University of Michigan, Ann Arbor, MI, USA. His current research interests include nonlinear, adaptive, robust, and predictive control theories and their applications to intelligent transportation, automotive, and energy systems.



Hao Wang received the B.E. degree in vehicle engineering from the Hefei University of Technology, Hefei, China, in 2012, and the M.S.E. degree in mechanical engineering from the University of Michigan, Ann Arbor, MI, USA, in 2014, where he is currently pursuing the Ph.D. degree in naval architecture and marine engineering.

His current research interests include set-membership identification and its applications, integrated energy management of power and thermal systems, and applications to electrified vehicles.



Xun Gong received the B.S. degree in electrical engineering from Northeast Electrical Power University, Jilin City, China, in 2010, and the Ph.D. degree in control theory and control engineering from Jilin University, Changchun, China, in 2016.

From 2013 to 2015 and 2016 to 2018, he was a Joint Ph.D. Student and a Post-Doctoral Researcher with the University of Michigan, Ann Arbor, MI, USA, respectively. His current research interests include model-based nonlinear control, optimal control, and control applications to connected automotive systems.



Dominic Liao-McPherson received the B.A.Sc. degree in engineering science, aerospace option, from the University of Toronto, ON, Canada, in 2015. He is currently pursuing the Ph.D. degree with the Department of Aerospace Engineering, University of Michigan, Ann Arbor, MI, USA.

His current research interests include constrained control, numerical methods, and algorithms for real-time optimization.



Ilya Kolmanovsky received the Ph.D. degree from the University of Michigan, Ann Arbor, MI, USA, in 1995.

He is currently a Professor with the Department of Aerospace Engineering, University of Michigan. His current research interests include control theory for systems with state and control constraints and control applications to aerospace and automotive systems.



Jing Sun received the Ph.D. degree from the University of Southern California, Los Angeles, CA, USA, in 1989.

From 1989 to 1993, she was an Assistant Professor with the Electrical and Computer Engineering Department, Wayne State University, Detroit, MI, USA. In 1993, she joined the Powertrain Control Systems Department, Ford Research Laboratory, Dearborn, MI, USA. In 2003, she joined the Faculty of the College of Engineering, University of Michigan, Ann Arbor, MI, USA, where she is currently the

Michael G. Parsons Professor and the Chair of the Department of Naval Architecture and Marine Engineering. Her current research interests include system and control theory and its applications to marine and automotive propulsion systems.